ChemPubSoc Europe

DOI: 10.1002/open.201600163

Open Access ChemistryOPEN Full Papers

Engineering Functions into Platinum and Platinum–Rhodium Nanoparticles in a One-Step Microwave Irradiation Synthesis

Maria Kalyva,* David S. Wragg, Helmer Fjellvåg, and Anja O. Sjåstad*[a]

Platinum (Pt) and platinum–rhodium (PtRh) nanoparticles (NPs) are active catalysts for a range of important industrial reactions, and their response has been shown to be affected by size, morphology, composition, and architectural configuration. We report herein the engineering of these functionalities into NPs by suitably modifying our single-step fabrication process by using microwave irradiation dielectric heating. NPs with different morphologies are acquired by manipulating the reaction kinetics with the concentration of the capping agent while keeping the reaction time constant. Pt@Rh core@shell octopod-cube, Pt-truncated-cube, and cube and small-sphere NPs having "near-monodisperse" distributions and average sizes in the range of 4 to 18 nm are obtained. By increasing the microwave time the composition of Pt@Rh can be tuned, and NPs with a Rh-rich shell and a tunable $Pt_{100-x}Rh_x$ ($x \leq 41$ at %) core are fabricated. Finally, alloy bimetallic PtRh NPs with controlled composition are designed by simultaneous tuning of the relative molar ratio of the metal precursors and the microwave irradiation time.

1. Introduction

Platinum-group metals (PGMs) are active catalysts for a variety of important industrial processes and technologies such as the Ostwald process (HNO_3 production), Andrussow oxidation for HCN synthesis, abatement catalysis (NO reduction and CO oxidation of flue gas of combustion of fuels), as well as for lower-temperature polymer electrolyte membrane fuel cells (PEMFCs). Currently, most of the processes involving HNO_3 and HCN production take place at elevated temperatures over expensive PtRh gauges. However, emerging technologies suggest that the replacement of PtRh gauges by PGM nanoparticles (NPs) deposited on an oxide support would allow the operation of the processes at less-aggressive temperatures.[1] Interestingly, an important functionality of the metal-supported catalyst is the architectural configuration of the metal component; for example, Pt@Rh core@shell particles are more active for CO oxidation than the corresponding alloy, a mixture of monometallic NPs, and pure Pt NPs.[2] For the preparation of metal-supported PGM catalysts, the routes outlined by An and Somorjai, allow superior tuning of the metallic particle size, morphology, and the elemental architectural distribution relative to classic impregnation techniques.[3] Nevertheless, fast, simple, and environmentally friendly routes for the production of well-tuned PGM NPs are necessary.

A number of chemical and physical synthesis approaches have been explored for the preparation of noble-metal NPs with controlled sizes, shapes, compositions, and configurations, including laser ablation, chemical reduction, UV photolysis, thermal decomposition, and metal vapor deposition.[4–8] These methods require specific setups, long processing timings, specific environmental conditions (e.g. gas atmospheres, high temperatures, etc.), and careful quenching of the reactions. In this perspective, microwave dielectric heating becomes an attractive technology for the rapid synthesis of inorganic NPs.[9] Several advantages of microwave heating contribute to greener nanosynthesis, including shorter reaction times, reduced energy consumption, and higher yields.[10]

Pt NPs with different shapes, such as nanorods and multipods, and sizes from 2 to 15 nm and average or poor distributions were previously prepared by microwave-assisted solvothermal synthesis by using polyvinylpyrrolidone (PVP) as a capping agent in conventional and scientific microwave ovens.[11–13] Control of Au planar nanostructures decorated with maghemite nanoparticles by PVP was reported by using a scientific microwave oven.[14] Near-monodisperse distributions of Rh, Pd, and Pt NPs were prepared recently by using PVP in a scientific microwave oven.[15] A wide variety of mono- and bimetallic nanoparticles containing Au, Ag, Pt, Pd, Ru, Rh, Cu, and Ni have been prepared by using a conventional microwave oven, giving either good or poor dispersions.[16] Lately, RhAg and RhAu NPs were prepared in good dispersions by using PVP and a scientific microwave oven.[17] Synthesis of

[a] Dr. M. Kalyva, Dr. D. S. Wragg, Prof. H. Fjellvåg, Prof. A. O. Sjåstad
Department of Chemistry, Centre for Materials Science and Nanotechnology
University of Oslo, Oslo 0315 (Norway)
E-mail: m.e.kalyva@smn.uio.no
a.o.sjastad@kjemi.uio.no

Supporting Information and the ORCID identification number(s) for the author(s) of this article can be found under http://dx.doi.org/10.1002/open.201600163.

core–shell Ru@Pt and Pt@Ru NPs by using microwave irradiation was reported, by successive reduction of the two precursors, which is today a quite universal method for core–shell NP preparation.[18–20] A systematic study involving engineering functionalities into Pt and PtRh NPs in an optimized single-step process by using a conventional microwave oven has not yet been reported.

We report herein a one-step microwave-assisted route for the preparation of Pt and PtRh NPs with diverse sizes, morphologies, compositions, and structural configurations by using a conventional microwave oven. By increasing the molar ratio of the PVP to metal precursors, a growth pattern for NPs with different morphologies was acquired by keeping the microwave time parameter fixed. Octopod-cube, truncated-cube, and cube and small-sphere NPs having "near-monodisperse" distributions and average sizes in the range of 4 to 18 nm were obtained. At the lowest amount of PVP, Rh was detected on the surface of the NPs, which was indicative of a core@shell configuration. Under these synthesis conditions and by increasing the microwave irradiation time, NPs with a Rh-rich shell and a tunable solid solution $Pt_{100-x}Rh_x$ ($x \leq 41$ at %) core were fabricated. Therefore, we standardized the parameter of microwave reaction time to the amount of Rh in solid solution with Pt of the NPs. Finally, alloy PtRh NPs with a controlled composition were prepared by simultaneously selecting the desired relative molar ratio of the precursors and suitable microwave time as standardized above, corresponding to the targeted solid solution concentration of Rh to Pt. The NPs were characterized by high-resolution transmission electron microscopy (HRTEM), energy-dispersive X-ray spectroscopy (HRTEM-EDS), powder X-ray diffraction (XRD), X-ray photoelectron spectroscopy (XPS), high-angle annular dark-field (HAADF) scanning transmission electron microscopy (STEM), and STEM-EDS line scan profiles.

2. Results and Discussion

Figure 1 presents the HRTEM images and histograms of the NPs produced by increasing the molar ratio of PVP to the metallic Pt and Rh precursors (equimolar amounts) from 0.007 to 0.28. In all cases, the total microwave irradiation time was fixed at 5 min. The HRTEM images of the octopod-cube NPs prepared with a molar ratio of 0.007 are shown in Figures 1 a, b. The corresponding histogram with an average nanoparticle size ($Đ$) of (17.9 ± 2.0) nm is presented in Figure 1 c; this histogram shows a "near-monodisperse" distribution, which is defined as particles having less than 0.15 coefficient of variation (CV) (i.e. $CV = \sigma / Đ$, in which σ and $Đ$ are the standard deviation and mean size, respectively).[21] From closer observation of the HRTEM images we see that there is a contrast difference around the NPs, which can be attributed to the mass contrast of Pt (atomic number 78) and Rh (atomic number 45). Increasing the molar ratio of PVP/precursors to 0.07 results in the formation of cubes (Figure 1 d, e), whereas the histogram (Figure 1 f) shows a "near-monodisperse" distribution with an average size of (7.1 ± 1.0) nm. Doubling the molar ratio to 0.14 results in the formation of truncated cubes as seen from the

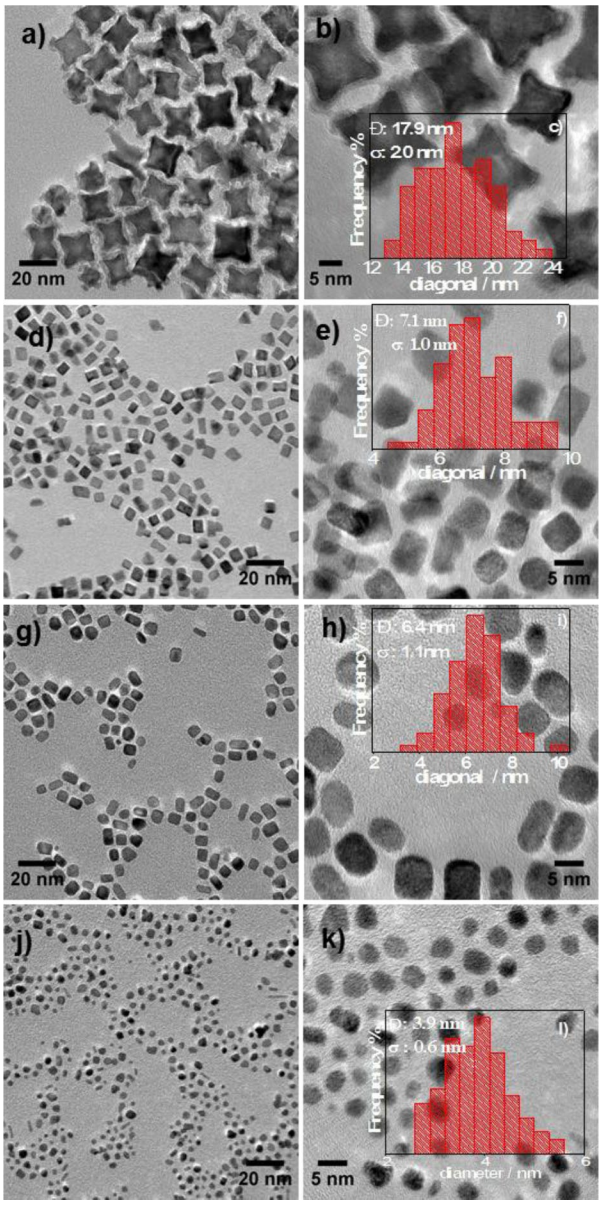

Figure 1. HRTEM images and the corresponding size-distribution histograms of a–c) octopod-cube, d–f) cube, g–i) truncated-cube, and j–l) spherical NPs prepared by increasing the PVP/metal precursors molar ratio.

HRTEM images (Figure 1 g, h) with a "near-monodisperse" distribution and $Đ = (6.4 \pm 1.0)$ nm, as seen in the histogram (Figure 1 i). Finally, by doubling the molar ratio of PVP/precursors to 0.28 we prepare small spheres (Figure 1 j, k) with a "near-monodisperse" distribution and an average size of (3.9 ± 0.6) nm, as seen in Figure 1 l.

Control of the size and morphology of Pt NPs such as cubes, cuboctahedra, octahedra, and other shapes was reported by adding a shape-control reagent, such as silver nitrate, during the chemical polyol reaction.[22] However, in this case there was a high risk of contaminating the NPs with the metal of the reagent. Affecting the reaction kinetics by changing the concentration of the capping agent is a simple and effective means to manipulate the growth process of the NPs, and thus to obtain nanocrystals with various morphologies. It was previously re-

ported that a growth pattern for AuPd NPs emerged upon increasing the time of the chemical polyol reaction leading to the formation of truncated cubes, to perfect cubes and finally to octopod-cube NPs, by increasing the amount of hexadecyltrimethylammonium chloride (CTAC) capping agent, which was shown to accelerate the reaction by producing a fast reduction rate of $[PdCl_4]^{2-}$.[23]

PVP is traditionally used in chemical polyol nanoparticles synthesis as a capping agent to limit particle growth and to prevent aggregation.[24] Similarly, in our experiments by increasing the amount of PVP the average particle size of the NPs was observed to decrease. However, the amount of PVP added is a critical parameter for the synthesis, because, as reported, an excess amount of PVP inhibits the reduction of precursors such as $H_2PtCl_6{\cdot}6H_2O$, which indirectly affects the kinetics of the chemical polyol reaction.[25] In this framework, we report herein, for the first time, Pt and PtRh NPs with different morphologies acquired by using microwaves, by keeping the reaction time constant and by decreasing the amount of PVP, which indirectly accelerates the reaction kinetics. Thus, we observe a growth pattern of the NPs and obtain small sphere shapes at the early stages of growth, and then truncated cubes, cubes, and finally octopod cubes.

Energy-dispersive X-ray spectroscopy (EDS) was employed to determine the chemical compositions of the NPs with different morphologies obtained by increasing the amount of PVP. The spectrum of the octopod-cube NPs shows the presence of characteristic X-ray PtMα and RhLα emissions; this spectrum is similar to that presented elsewhere for bimetallic PtRh NPs, which reveals the coexistence of Pt and Rh (Figure 2a).[26,27] The atomic percentage of Rh is calculated to be 20 at%, which is not in agreement with the nominal equimolar ratio used for the synthesis. The spectra acquired for the cubes, truncated cubes, and small spheres show only the presence of Pt (Figure 2b–d).

Figure 3a presents the powder X-ray diffraction patterns of the octopod-cube, cube, truncated-cube, and spherical NPs. All the differently shaped NPs present strong diffraction peaks at $2\theta \approx 39.8$, 46.4, and 67.6° that can be indexed to the (111), (200), and (220) planes of face-centered cubic (fcc) pure platinum.[28,29] The patterns were fitted by TOPAS software, and the crystallite size of the NPs for the octopod-cube, cube, truncated-cube, and spherical NPs were found to be (13.3 ± 0.1), (6.1 ± 0.1), (5.2 ± 0.1), and (4.0 ± 0.3) nm, respectively. These values are close to the average particle sizes originating from TEM analysis, except for the size of the octopod-cube PtRh NPs. Closer observation of the XRD peak of the octopod-cube

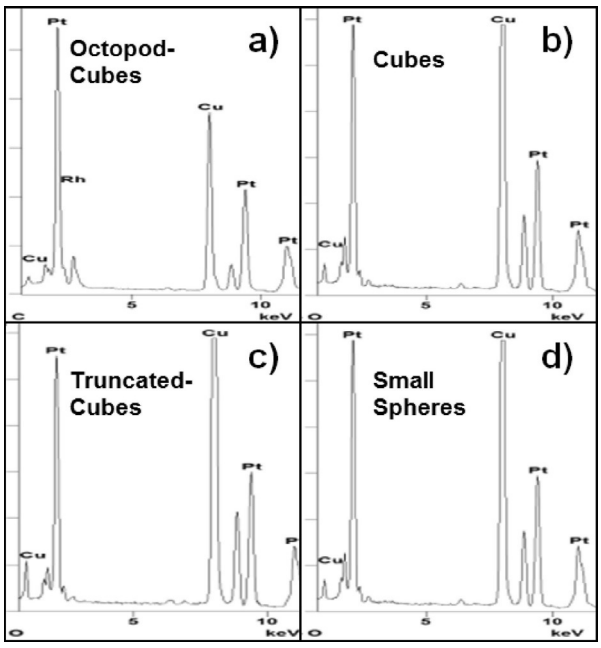

Figure 2. HRTEM-EDS spectra originating from a) octopod-cube, b) cube, c) truncated-cube, and d) spherical NPs prepared by increasing the PVP/metal precursors molar ratio.

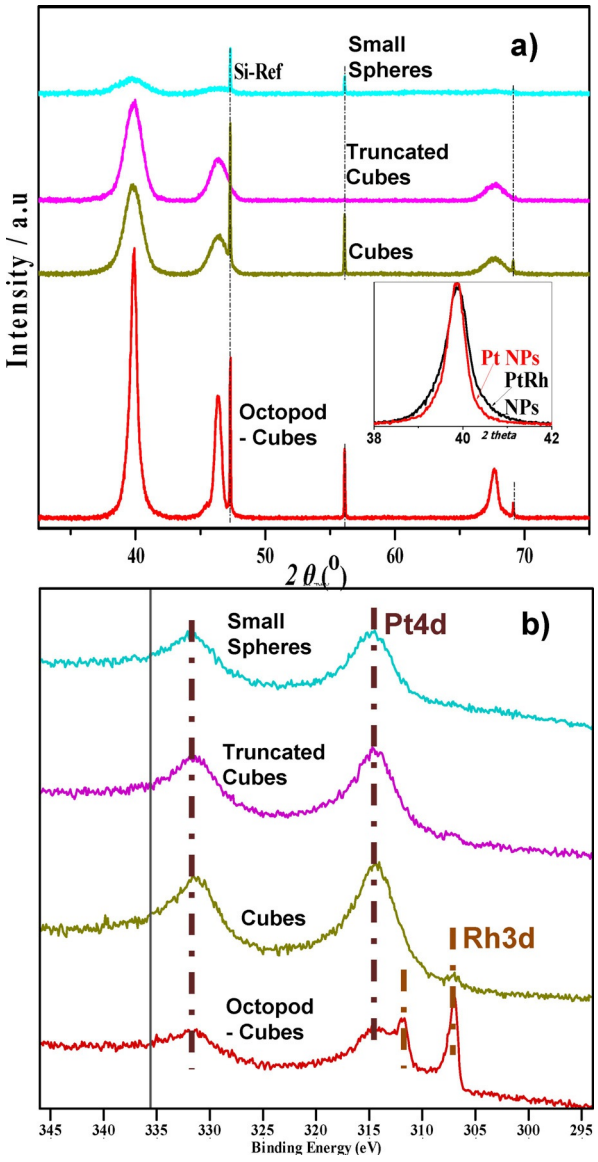

Figure 3. a) XRD patterns of octopod-cube, cube, truncated-cube, and spherical NPs [inset: 2θ XRD (111) of the Pt and PtRh octopod-cube NPs] and b) Pt 4d and Rh 3d XPS peaks of the corresponding NPs drop casted on SiO_2 wafers.

PtRh NPs shows no considerable shift, but the bottom of the peak appears to be broader than that of the Pt NPs prepared under the same conditions, as can be seen from the inset of Figure 3a. As such, the fitting of this XRD pattern is complicated, and this leads to a smaller size than the corresponding size originating from TEM analysis. These differences are indicative of the presence of a very small NP population, which is formed on the outer part or around the octopod-cube NPs, as carefully seen from the HRTEM images (Figure 1a, b). As mentioned above, only in the case of octopod-cube NPs is Rh detected by EDS (Figure 2a). The combination of the HRTEM, EDS, and XRD results suggest that Rh is formed on top of Pt octopod-cube NPs to form a Pt@Rh core@shell structure.

To further elucidate the chemical composition of the NPs, XPS measurements were performed. Figure 3b presents the XPS Pt 4d and Rh 3d peaks originating from the octopod-cube, cube, truncated-cube, and spherical NPs.

Only in the case of octopod-cube NPs are Rh 3d XPS peaks detected, in agreement with the corresponding EDS results (Figure 2). The atomic ratio of Pt/Rh for the octopod-cube NPs can be calculated by using the integrated area of the Pt $4d_{5/2}$ to Rh $3d_{5/2}$ XPS peaks as well as their relative sensitivity factors; a similar procedure for the calculation of the composition of PtRh NPs was used elsewhere.[30] Using the Pt/Rh atomic ratio, we can estimate that the NPs contain about 45 at% Rh, which is considerably more than that calculated by EDS ($\approx$20 at%).

Given that XPS is a surface-sensitive technique able to detect a signal from up to the first 10 nm and that the octopod-cube NPs have an average size of 18 nm, the high Rh concentration calculated by XPS suggests that Rh is formed on the surface of the NPs.[31]

At the lowest amount of PVP, we observed that the formation of the Pt@Rh NPs structure was favored, and thus, we increased the microwave time up to 20 min to explore the possibility of tuning the composition of the core@shell NPs. Figure 4 shows the HRTEM images and the corresponding EDS spectra of the NPs produced by microwave irradiation for 7, 10, 15, and 20 min by keeping all other parameters constant.

In all cases, we observe that the NPs are dispersed but that their shapes are irregular and cannot be controlled. The EDS measurements demonstrate that as the microwave time increases, the Rh content also increases. The values of Rh (at%) are listed inTable 1.

By increasing the microwave time, more Rh precipitates on top of the Pt@Rh NPs, and simultaneously, a thermally activated diffusion process is highly possible at longer reaction times.[32] However, Rh diffusion on non-spherical Pt NPs is not likely to proceed uniformly, and this creates a large strain in the structure of bimetallic NPs. According to Buffat et al., small metal particles are able to accommodate large amounts of strain, often through the formation of irregular polycrystalline structures and lattice defects, which can explain the observed irregular shapes of our NPs.[33]

Figure 5a presents the XRD patterns of the PtRh NPs produced by microwave irradiation for 7, 10, 15, and 20 min.

The XRD patterns of the pure Pt (bottom pattern) and Rh (upper pattern) NPs prepared by microwave irradiation are included in Figure 5a for comparison. The XRD pattern of the pure Rh nanoparticles (upper pattern) shows diffraction peaks at $2\theta \approx 41$, 47, and 69.3° that are indexed to the (111), (200), and (220) planes of the fcc structure; these values are higher than those of the pure Pt NPs mentioned above due to the slightly larger metallic radius of Pt, in agreement with the literature.[34] The lattice parameters of the pure Pt and Rh NPs were calculated by using TOPAS software to be (3.9171 $\pm$ 0.0001) and (3.8351 $\pm$ 0.0001) Å, respectively, which deviate from the reported bulk values (Pt bulk 3.9231 Å and Rh bulk 3.8032 Å).[35–37] Similarly, larger lattice constant values were reported for Rh NPs for sizes $<$10 nm, and that was attributed to the surface strain of such small NPs.[38]

Upon increasing the microwave irradiation time to 7, 10, 15, and 20 min, the XRD 2θ peaks are shifted to higher angles relative to the values of pure Pt, and the (111) plane is found at $2\theta = 39.9$, 40.1, 40.2, and 40.3°, respectively. The lattice parameter values of the produced NPs at the longer microwave times were calculated by using TOPAS software and are listed in Table 2.

By increasing the microwave time we observe lattice contraction, which arises from substitution of the smaller Rh atoms by larger Pt atoms in a controlled manner. Upon heating, the Rh shell, which has a larger proportion of surface

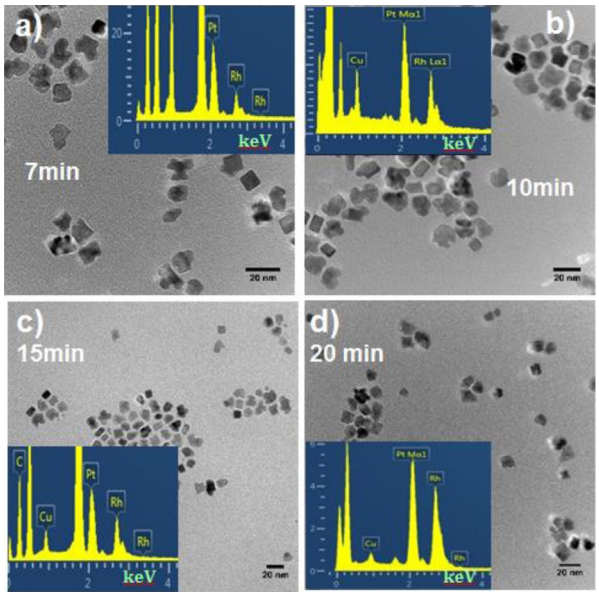

Figure 4. HRTEM images and EDS spectra of NPs prepared with microwave irradiation times of a) 7, b) 10, c) 15, and d) 20 min.

Table 1. Rh contents in PtRh NPs at various microwave times, as determined by EDS, XPS, and XRD.

Microwave time [min]	Rh content [at%]		
	EDS	XRD	XPS
7	22	16	45
10	31	25	52
15	44	32	57
20	47	41	65

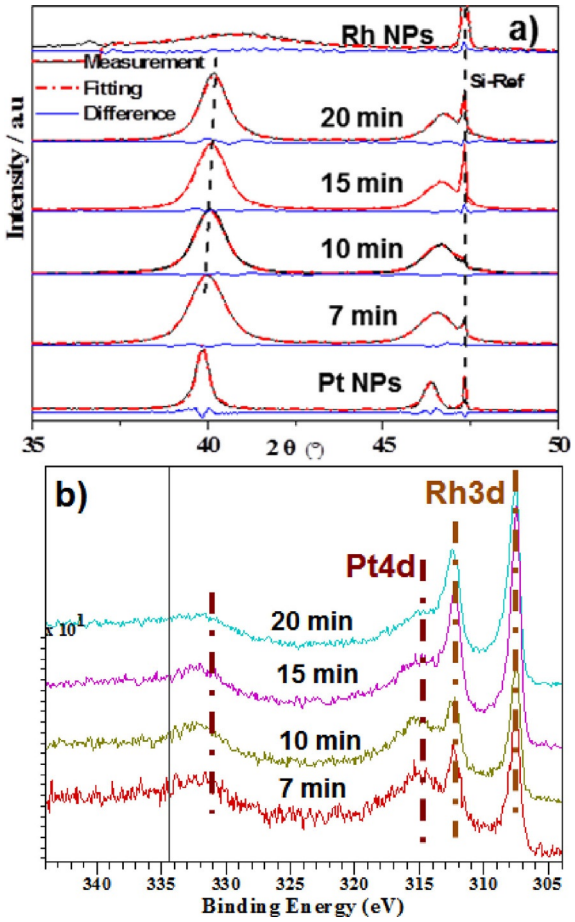

Figure 5. a) XRD patterns of NPs with a Rh-rich shell and a tunable $Pt_{100-x}Rh_x$ ($x \leq 41$ at%) core prepared with microwave irradiation times of 7, 10, 15, and 20 min (bottom and top pattern correspond to the pure Pt and Rh NPs, respectively) and b) Pt 4d and Rh 3d XPS peaks of the corresponding NPs drop casted on SiO_2 wafers.

Table 2. Lattice constant of NPs with a Rh-rich shell and a tunable $Pt_{100-x}Rh_x$ ($x \leq 41$ at%) core at various microwave times.

Microwave time [min]	Lattice constant a [Å][a]
7	3.9016 ± 0.0003
10	3.8952 ± 0.0003
15	3.8907 ± 0.0003
20	3.8830 ± 0.0005

[a] Rietveld method performed by TOPAS-5 and Stephens model.

atoms, will experience large surface stress, and therefore would be more affected than the Pt core. This will provide the driving force for the thermal diffusion of the Rh atoms into the Pt core, and nanoscale alloying will take place to form a diffusion layer initially composed of a small amount of Rh atoms doped into the Pt lattice. As the time increases, diffusion proceeds, which continuously drives the outside Rh atoms into the diffusion layer and into the interior Pt core. A similar process was reported by studying the thermal diffusion in bimetallic Cu@Au NPs.[39]

The Rh-rich fcc solid solution that is formed can be quantified by using Vegard's law and our calculated lattice parameters for pure Pt and Rh NPs. The values of Rh (at%) from the XRD analysis are presented in Table 1. In good agreement with our results, shifts in the (111) peak at $2\theta = 40.2$ and 40.3° were reported for bimetallic PtRh NPs chemically synthesized having an increased Rh content of PtRh(3:1) and PtRh(2:1), respectively.[40] Additionally, the lattice parameter of chemically synthetized Pt_5Rh NPs with a Rh content of about 15 at% was reported to be $a = 3.904$ Å; the lattice parameter and Rh content of the NPs produced with a microwave time of 7 min in our experiments, were similarly found to be $a = 3.902$ Å and 16 at%, respectively.[41] Therefore, we were able to standardize the parameter of microwave reaction time with the amount of Rh forming a solid solution with Pt into the NPs.

It is evident that the EDS values show a higher Rh content than the corresponding XRD values. Given that the calculated XRD values represent the percentage of Rh alloying in solid solution with Pt and because we observed that Rh nucleates slower, we postulate that the additional amount of Rh found by EDS is formed on the surface of the NPs.

Figure 5b shows the XPS Pt 4d and Rh 3d peaks of the NPs produced by microwave irradiation for 7, 10, 15, and 20 min. After 7 min of microwave time, the Rh content calculated from the XPS peaks is about 46 at%, which is similar to the percentage calculated at 5 min, as shown in Table 1. For the NPs produced at 10, 15, and 20 min, the Rh contents, as determined by XPS, are increasing, as shown in Table 1. The Rh contents calculated by XPS for all of the synthesis, are higher than those calculated by EDS and XRD. Therefore, by keeping an equimolar concentration of the precursors and by increasing the microwave time, we were able to fabricate NPs with a Rh-rich shell and a tunable $Pt_{100-x}Rh_x$ ($x \leq 41$ at%) core.

Co-reduction of metal precursors with different standard reduction potentials [electrode potentials with respect to the standard hydrogen electrode (SHE)] was reported as a method for the preparation of core@shell NPs in a one-pot chemical synthesis route.[42] However, even though a variety of noble-metal Pt@Ag, Ru@Ag, Pt@Au, and Rh@Au NPs were prepared from metal precursors having different standard reduction potentials, the co-reduction of K_2PtCl_4 and $RuCl_3$, which have different standard reduction potentials (0.755 V for $PtCl_4^{2-}$ and 0.2487 V for Ru^{3+}), leads to the formation of an alloy structure. Therefore, the reduction kinetics of different metal precursors is highly sensitive to the environment of the chemical reaction, including solvents, surfactants, and temperature, and it is rather impossible to predict the structure of the NPs just by knowing the reduction potential values. In contrast, in our synthesis the reduction potentials of the Pt and Rh precursors are similar (0.76 V for $PtCl_4^{2-}$ and 0.75 V for Rh^{3+}); however, the formation of the core@shell NPs structure seems to be favored.[43] Thus, we evidenced experimentally and report here for the first time the formation of core@shell NPs having a Rh-rich shell and a tunable core composition with up to 41 at% Rh in a one-step synthesis by using microwaves.

Bimetallic PtRh alloy NPs with a controlled composition were designed by selecting the desired relative molar ratio of the metal precursors and by choosing the standardized microwave reaction time known to facilitate the desired Rh concen-

tration in a solid solution phase with Pt. For example, to prepare $Pt_{90}Rh_{10}$ solid solution alloy NPs, we chose the Pt/Rh metal precursor ratio to be 90:10 and the microwave time to be 7 min, for which it was shown by XRD that the NPs contained around 16 at% Rh. The HRTEM image of the NPs prepared under the aforementioned conditions and the histogram in the inset originating from these images show spherical NPs with a "near-monodisperse" distribution with $\bar{D} = (3.8 \pm 0.6)$ nm (Figure 6a).

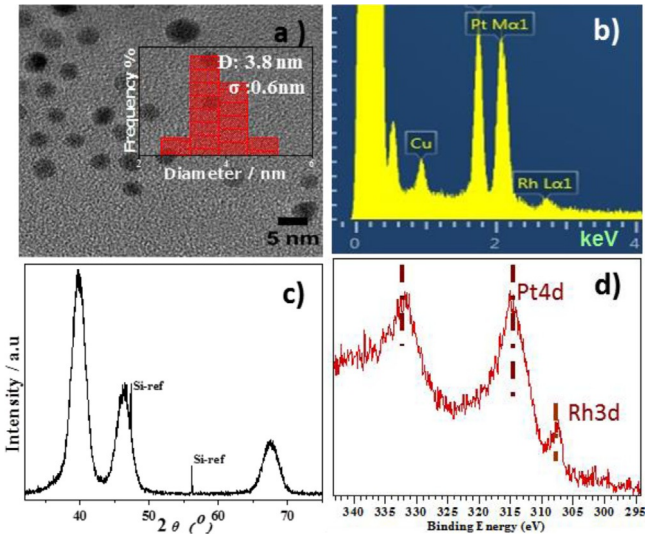

Figure 6. a) HRTEM image (inset: histogram of the size distribution of the NPs), b) EDS results, c) XRD pattern, and d) XPS spectrum of $Pt_{90}Rh_{10}$ alloy NPs prepared with a microwave irradiation time of 7 min.

The EDS results show the presence of both Pt and Rh, whereas the calculated atomic percentage of Rh is found to be 12 at%, which is very close to the starting precursor ratio used for the synthesis (Figure 6b). In total agreement, the XRD pattern shows a shift in the 2θ angles that correspond by Vegard's law to a Rh content of 10 at% (Figure 6c). Figure 6d shows the XPS peaks of Pt 4d and Rh 3d, and the calculated content of Rh to be about 11 at%. Therefore, as all the techniques that were used to characterize the NPs either in bulk or on the surface are in agreement with the starting molar ratio of the precursors for the synthesis, the formation of alloy $Pt_{90}Rh_{10}$ NPs with engineered composition is supported.

High-angle annular dark-field (HAADF) scanning transmission electron microscopy (STEM) images and STEM-EDS line scan profiles on a single and few NPs are presented in Figure 7. These measurements were performed, as it is possible to characterize and differentiate the various architectural configurations and local compositions of the core@shell and alloy NPs.[44,45]

Figure 7a shows a HAADF-STEM image of the core@shell NPs prepared with an equimolar concentration of the precursors and a total microwave time of 20 min. It is evident that the NPs are composed of a dark contrast core part and a lighter contrast shell part. Given that Pt atoms are significantly heavier than Rh atoms, the mass contrast reveals a core@shell configu-

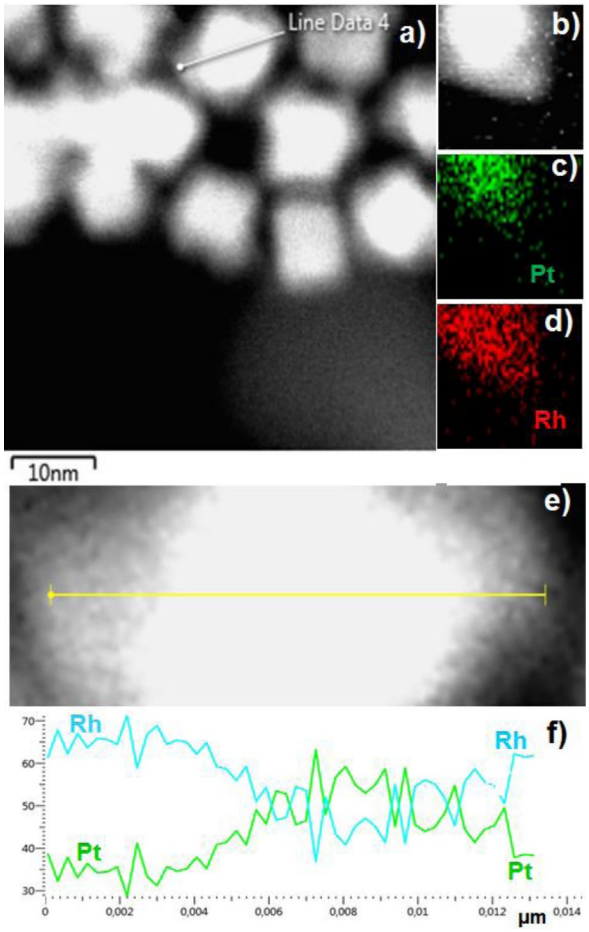

Figure 7. HAAD-STEM electron image a) of a few NPs, b) of one NP produced with a microwave irradiation time of 20 min, c,d) corresponding STEM-EDS mapping images with selected colors for Pt and Rh, and e,f) STEM-EDS line scan profile.

ration of the NPs.[46] Figure 7b shows a HAADF-STEM image of one NP, and Figure 7c,d shows the corresponding elemental mapping images from PtMα and RhLα emissions.[47] Similarly, a deficiency of Pt in the outer layer of the NP is revealed, which confirms the local architecture to be a core@shell structure. Figure 7e,f presents the HAADF image and the corresponding STEM-EDS line scan profile of one NP, from which the local Rh content can be distinguished across the NP. It is interesting to note that, in the shell part of the NP, the Rh content is about 65 at%, which is in good agreement with our calculated value from the XPS measurements, and that in the core part it is around 40 at%, which is similar to the calculated value from the XRD results. Therefore, we present here complete characterization of the fabricated NPs, for which the results show good agreement among the complementary techniques.

Figure 8a shows a HAADF-STEM image of alloy $Pt_{90}Rh_{10}$ NPs, for which there is no evident mass contrast difference on the NPs.

The HAADF-STEM image and the corresponding EDS line scan profile of two $Pt_{90}Rh_{10}$ NPs are seen in Figure 8b,c. Notably, the composition across the NPs is constant with a Rh content of about 10 at%, which is similar to the starting composi-

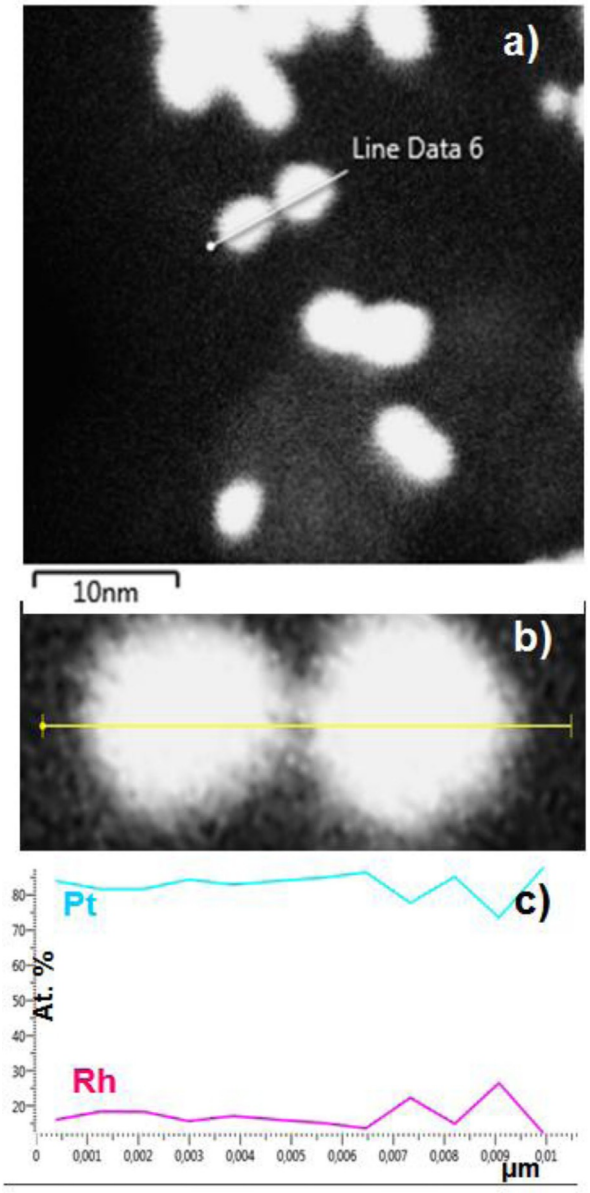

Figure 8. HAAD electron image of a) alloy $Pt_{90}Rh_{10}$ NPs, b) two NPs, and c) their STEM-EDS line scan profiles.

tion of the metal precursors of the synthesis, revealing the preparation of an alloyed structure with controlled composition.

3. Conclusions

In summary, a fast, facile, and versatile method was developed by which a variety of functions, such as size, morphology, composition, and structural configuration, can be engineered into Pt and PtRh nanoparticles (NPs) in a conventional microwave oven. Manipulating the reaction kinetics by tuning the amount of capping agent, polyvinylpyrrolidone (PVP), we were able to tune the morphology of the NPs by using microwaves. We acquired octopod-cube, cube, truncated-cube, and spherical NPs with average sizes of 18, 7, 6, and 4 nm, respectively, in "near-monodisperse" distributions. Only with the lowest amount of PVP was Rh detected on the surface of the Pt NPs, which indicated the formation of Pt@Rh core@shell NPs. Under these synthesis conditions, by increasing the microwave time, NPs with a Rh-rich shell and a tunable $Pt_{100-x}Rh_x$ core with a Rh content up to 41 at% were prepared. Finally, bimetallic alloy PtRh NPs with controlled compositions were designed by simultaneous tuning of the relative molar ratio of the metal precursors and the microwave time, which proved the versatility of our synthesis method. Therefore, we managed to modify and optimize our fabrication route in a controlled manner, and through a single-step process involving the use of microwaves, we essentially designed NPs with custom-made functionalities that may lead to specialized performances.

Experimental Section

Chemicals and Materials

Rhodium(III) acetylacetonate [$Rh(acac)_3$, 97%], platinum(IV) chloride ($PtCl_4$, +99.9%), oleylamine (OAm, tech. 70%), polyvinylpyrrolidone (PVP) with an average molecular weight of 10000, and *N*,*N*-dimethylformamide (DMF, 99.8%) were purchased from Sigma–Aldrich. Ethanol and toluene of analytical-reagent grade were used for all experiments.

Synthesis of Pt and PtRh NPs

In a typical synthesis, the metallic precursors (both 0.145 mmol) were dissolved in DMF (2 mL) and were then mixed with OAm (4.2 mL) and varying amounts of PVP. OAm acted as both the reducing agent and the capping material,[16] whereas PVP acted as a capping agent. Residual organic molecules on the surface of the Pt NPs upon using PVP or/and OAm during the synthesis was previously reported.[48] The mixture was kept in an oil bath under continuous stirring at a temperature of 100 °C until a clear solution was obtained. The clear solution was placed in a conventional Miele M8201 microwave oven operating at 900 W. Given that conventional microwave ovens lack armoring of the cavity, which can protect against possible explosions, careful assessment of experimental safety in terms of materials selection and procedures should be performed. The total microwave irradiation time was varied from 5 to 20 min in "on for 30 s" followed by "off for 5 s" time cycles and stirring on a hot plate outside the microwave oven. After cooling down slowly in air, the nanocrystals were obtained by flocculating the reaction solution in ethanol followed by particle separation by using a centrifuge operating at 5000 rpm for 5 min. At a microwave time of 20 min, the color of the supernatant after centrifugation was a weak pale yellow, which showed that a small amount of Rh had not reacted, as the Rh precursor has a strong yellow color. The particles were washed at least two times with ethanol and ethanol/toluene mixtures before re-dispersing in toluene (10 mL).

Powder X-ray diffraction Characterization

The powder X-ray diffraction (XRD) patterns were collected at room temperature with a Bruker D8 Discover diffractometer equipped with a Ge(111) monochromator, which gave CuKα1 radiation ($\lambda = 1.5406$ Å) and a position-sensitive LynxEye detector. The free-standing NPs were deposited on specially cut Si single-crystal zero-background holders. Analysis of the diffraction patterns by

the Rietveld method was performed by using the TOPAS version 5, Bruker AXS 2015, and NIST silicon powder [SRM 640d, $a = (5.43123 \pm 0.00008)$ Å] as an internal standard for sample height correction.[49] Crystallite sizes were calculated by using the double Voigt method to obtain column heights (Lvol-IB in TOPAS).[50] The Stephens method was used to improve the fitting of *hkl*-dependent peak broadening; however, despite clear improvements in visual fit quality and R_{wp}, the use of the Stephens model had a negligible effect (less than one estimated standard deviation) on the lattice parameters and crystallite sizes (as seen in Table S1 in the Supporting Information).[51]

Sample Characterization by HRTEM-EDS

High-resolution transmission electron microscopy (HRTEM) images were acquired with a JEOL JEM-2100F microscope operating at 200 kV and equipped with a Gatan Orius SC 200D 2, 14 bit, 11 megapixel CCD and a spherical aberration corrector in the objective lens to ensure a point resolution of 1.2 Å. An Oxford Inca energy-dispersive silicon-drift X-ray (EDS), X-Max^N 80 T spectrometer was provided for compositional analysis. For every sample, the EDS measurements were acquired in five different areas of the grid and on top of a couple of NPs each time, and the average values are presented. All the samples for HRTEM analysis were prepared by drop casting 30 μL of the prepared solution onto carbon-coated, 300 mesh, 3 mm copper grids, Agar Scientific UK, and then allowing to dry under an inert atmosphere. The diameter or the diagonal of more than 250 NPs, depending on their shape shown in the HRTEM images, were measured each time to estimate their distribution (size distribution) by using Image J software. High-angle annular dark-field (HAADF) STEM images and STEM-EDS line scan profiles on single NPs were performed by using a 0.7 nm EDS probe in the STEM mode.

XPS Measurements of the NPs

XPS analysis of the samples was performed with a Kratos Axis Ultra^{DLD} instrument by using monochromatic AlKα radiation ($h\nu = 1486.6$ eV) at 15 kV and 10 mA. The pass energies for the survey and high-resolution scan were 160 and 20 eV, respectively. The pressure in the chamber was maintained below of 6×10^{-9} Torr during the analysis. The binding-energy values were corrected with reference to C 1s = 284.6 eV.

Acknowledgements

Research leading to these results received funding from the Research Council of Norway (TOPCat project, GASSMAX, Grant number 2155461/E30). The authors would like to thank Dr. Stefano Rubino for his help for HRTEM characterization.

Conflict of Interest

The authors declare no conflict of interest.

Keywords: alloys · microwave chemistry · nanoparticles · platinum · rhodium

[1] J. Schäffer, V. A. Kondratenko, N. M. Steinfeldt, M. Sebek, E. V. Kondratenko, *J. Catal.* **2013**, *301*, 210 – 216.
[2] S. Alayoglu, B. Eichhorn, *J. Am. Chem. Soc.* **2008**, *130*, 17479 – 17486.
[3] K. An, G. A. Somorjai, *ChemCatChem* **2012**, *4*, 1512 – 1524.
[4] M. Kalyva, G. Bertoni, A. Milionis, R. Cingolani, A. Athanassiou, *Microsc. Res. Tech.* **2010**, *73*, 937 – 943.
[5] J. Turkevich, G. Kim, *Science* **1970**, *169*, 873 – 879.
[6] K. Torigoe, K. Esumi, *Langmuir* **1993**, *9*, 1664.
[7] K. Esumi, T. Tano, K. Torigoe, K. Meguro, *Chem. Mater.* **1990**, *2*, 564 – 567.
[8] K. J. Klabunde, Y. X. Li, B. J. Tan, *Chem. Mater.* **1991**, *3*, 30 – 39.
[9] I. Bilecka, M. Niederberger, *Nanoscale* **2010**, *2*, 1358 – 1374.
[10] J. A. Dahl, B. L. S. Maddux, J. E. Hutchison, *Chem. Rev.* **2007**, *107*, 2228.
[11] N. N. Mallikarjuna, R. S. Varma, *Cryst. Growth Des.* **2007**, *7*, 686 – 690.
[12] D. Li, S. Komarneni, *Z. Naturforsch. B* **2006**, *61*, 1566 – 1572.
[13] L. Dai, Q. Chi, Y. Zhao, H. Liu, Z. Zhou, J. Li, T. Huan, *Mater. Res. Bull.* **2014**, *49*, 413.
[14] J. A. Hachtel, S. Yu, A. R. Lupini, S. T. Pantelides, M. Gich, A. Laromaine, A. Roig, *Faraday Discuss.* **2016**, *191*, 215.
[15] N. Dahal, S. Garcıa, J. Zhou, S. M. Humphrey, *ACS Nano* **2012**, *6*, 9433 – 9446.
[16] V. Abdelsayed, A. Aljarash, M. Samy El-Shall, Z. A. Al Othman, A. H. Alghamdi, *Chem. Mater.* **2009**, *21*, 2825.
[17] S. Garcıa, L. Zhang, G. W. Piburn, G. Henkelman, S. M. Humphrey, *ACS Nano* **2014**, *11*, 11512 – 11521.
[18] M. Miyakawa, N. Hiyoshi, M. Nishioka, H. Koda, K. Sato, A. Miyazawa, T. M. Suzuki, *Nanoscale* **2014**, *6*, 8720 – 8725.
[19] L. Zhang, J. Kim, J. Zhang, F. Nan, N. Gauquelin, G. A. Botton, P. He, R. Bashyam, S. Knights, *Appl. Energy* **2013**, *103*, 507 – 513.
[20] L. Zhang, J. Kim, H. M. Chen, F. Nan, K. Dudeck, R. S. Liu, G. A. Botton, J. Zhang, *J. Power Sources* **2011**, *196*, 9117 – 9123.
[21] H. Cui, Y. Feng, W. Ren, T. Zeng, H. Lv, Y. Pan, *Recent Pat. Nanotechnol.* **2009**, *3*, 32 – 41.
[22] N. V. Long, N. D. Chien, T. Hayakawa, H. Hirata, G. Lakshminarayana, M. Nogami, *Nanotechnology* **2010**, *21*, 035605.
[23] J. Li, Y. Zheng, J. Zeng, Y. Xia, *Chem. Eur. J.* **2012**, *18*, 8150 – 8156.
[24] H. Hei, H. He, R. Wang, X. Liu, G. Zhang, *Soft Nanosci. Lett.* **2012**, *2*, 34.
[25] J. M. Petroski, Z. L. Wang, T. C. Green, M. A. El-Sayed, *J. Phys. Chem. B* **1998**, *102*, 3316.
[26] N. Savastenko, H. R. Volpp, O. Gerlach, W. Strehlau, *J. Nanopart. Res.* **2008**, *10*, 277 – 287.
[27] A. Cao, G. Veser, *Nat. Mater.* **2010**, *9*, 75 – 81.
[28] N. V. Long, C. M. Thi, M. Nogami, M. Ohtaki, *New J. Chem.* **2012**, *36*, 1320 – 1334.
[29] J. Zeng, *J. Mater. Chem.* **2012**, *22*, 3170 – 3176.
[30] J. Y. Park, Y. Zhang, M. Grass, T. Zhang, G. A. Somorjai, *Nano Lett.* **2008**, *8*, 673 – 677.
[31] D. Briggs, M. P. Seah, *Practical Surface Analysis, Auger and X-ray Photoelectron Spectroscopy, Vol. 1* (Eds.: D. Briggs, M. P. Seah), Wiley, New York, **1990**, pp. 1 – 16.
[32] R. Ferrando, J. Jellinek, R. L. Johnston, *Chem. Rev.* **2008**, *108*, 845 – 910.
[33] P. A. Buffat, *Mater. Chem. Phys.* **2003**, *81*, 368.
[34] B. R. Sathe, *RSC Adv.* **2013**, *3*, 5361 – 5365.
[35] T. Ioroi, K. J. Yasuda, *Electrochem. Soc.* **2005**, *152*, A1917.
[36] A. R. Denton, N. W. Ashcroft, *Phys. Rev. A* **1991**, *43*, 3161.
[37] E. Antolini, F. Colmati, E. R. Gonzalez, *J. Power Sources* **2009**, *193*, 555.
[38] P. Müller, U. Hejral, U. Rutta, A. Stierle, *Phys. Chem. Chem. Phys.* **2014**, *16*, 13866.
[39] S. Liu, Z. Sun, Q. Liu, L. Wu, Y. Huang, T. Yao, J. Zhang, T. Hu, M. Ge, F. Hu, Z. Xie, G. Pan, S. Wei, *ACS Nano* **2014**, *8*, 1886 – 1892.
[40] K. W. Park, D. S. Han, Y. E. Sung, *J. Power Sources* **2006**, *163*, 82.
[41] B. Liu, Z. W. Chia, C. H. Cheng, J. Y. Lee, *Energy Fuels* **2011**, *25*, 3135 – 3141.
[42] P. Hou, H. Liu, J. Li, J. Yang, *CrystEngComm* **2015**, *17*, 1826.
[43] A. J. Arvia, D. Posadas, N. Maki, N. Tanaka, *Standard Potentials in Aqueous Solutions* (Eds.: A. J. Bard, R. Parsons, J. Jordan), Marcel Dekker, Inc., New York, **1985**, pp. 321 – 377.
[44] S. A. Alayoglu, B. Eichhorn, *J. Am. Chem. Soc.* **2008**, *130*, 17479 – 17486.
[45] Z. Peng, H. You, H. Yang, *Adv. Funct. Mater.* **2010**, *20*, 3734 – 3741.
[46] P. Strasser, S. Koh, T. Anniyev, J. Greeley, K. More, C. Yu, Z. Liu, S. Kaya, D. Nordlund, H. Ogasawara, M. F. Toney, A. Nilsson, *Nat. Chem.* **2010**, *2*, 454.

[47] F. Tao, M. E. Grass, Y. Zhang, D. R. Butcher, F. Aksoy, S. Aloni, V. Altoe, S. Alayoglu, J. R. Renzas, C. K. Tsung, Z. Zhu, Z. Liu, M. Salmeron, G. A. Somorjai, *J. Am. Chem. Soc.* **2010**, *132*, 8697 – 8703.
[48] C. Kim, M. Min, Y. W. Chang, K.-H. Yoo, H. Lee, *J. Nanosci. Nanotechnol.* **2010**, *10*, 233 – 239.
[49] H. M. Rietveld, *J. Appl. Crystallogr.* **1969**, *2*, 65 – 71.
[50] D. Balzar, N. Audebrand, M. R. Daymond, A. Fitch, A. Hewat, J. I. Langford, A. Le Bail, D. Louër, O. Masson, C. N. McCowan, N. C. Popa, P. W. Stephens, B. H. Toby, *J. Appl. Crystallogr.* **2004**, *37*, 911 – 924.
[51] P. W. Stephens, *J. Appl. Crystallogr.* **1999**, *32*, 281 – 289.

Received: December 1, 2016
Revised: January 19, 2017
Published online on February 28, 2017

